Low-Dimension Angular Representation for Near-Field LoS Extra-Large MIMO Channel

Anzheng Tang[*], Jun-Bo Wang[*], Yijian Chen[†], Hongkang Yu[†], Yijin Pan[*],
Wence Zhang[‡], and Rodrigo C. de Lamare[§]
[*]National Mobile Communications Research Lab, Southeast University, Nanjing 210096, China.
[†]Wireless Product Research and Development Institute, ZTE Corporation, Shenzhen 518057, China.
[‡]School of Computer Science and Communication Engineering, Jiangsu University, Zhenjiang 212013, China.
[‡]Department of Electronic Engineering, University of York, York YO10 5DD, U.K.
Email: {anzhengt, jbwang, panyj}@seu.edu.cn, {yu.hongkang, chen.yijian}@zte.com.cn,
wencezhang@ujs.edu.cn, and delamare@cetuc.puc-rio.br

Abstract—**With the combination of extra-large arrays and high frequencies, near-field transmission has become prevalent. In this paper, we investigate the angular-domain representation of the near-field line-of-sight (LoS) channel. Specifically, we first demonstrate the structured sparsity of the near-field LoS channel in the angular domain. Building upon this sparsity, we propose an effective spatial bandwidth channel representation method. This method characterizes the near-field LoS XL-MIMO channel as a superposition of multiple virtual far-field LoS paths, thereby capturing the spherical wavefront effect within a low-dimensional angular channel. Finally, simulations validate the equivalence between the proposed representation and the existing antenna-domain channel model.**

I. INTRODUCTION

The increasing demand for data transmission rate in present and future wireless communication systems necessitates revolutionary advancements to support emerging applications such as holographic video, virtual reality, and digital twins. To meet these requirements, the deployment of extra-large multiple-input-multiple-output (XL-MIMO) systems operating in high-frequency bands has been widely recognized as a critical technology [1], [2]. However, the combination of extra-large arrays and high frequencies introduces new electromagnetic (EM) wave propagation characteristics.

Unlike massive MIMO systems, with the dramatically increasing number of antennas in XL-MIMO communication systems, receivers may lie in the near-field region of the transmitter [3]. Consequently, the spherical wavefront effect cannot be ignored. On the other hand, in the mmWave and sub-THz bands, multipath propagation is significantly weaker due to the lack of diffraction and surface roughness as compared to the wavelength [4], which results in the LoS path becoming the dominant propagation component. Consequently, there is a great deal of interest in exploring the potential of near-field LoS XL-MIMO systems.

For example, the authors of [5] analyzed the optimal communication modes for extra-large arrays and derived analytical expressions for the LoS link gain and available spatial degrees of freedom (DoFs). The authors of [6] developed an analytical framework based on spatial bandwidth analysis to reveal the impact of the array geometries on the achievable spatial DoFs. The authors of [7] investigated the spatial DoFs of LoS MIMO via intelligent reflecting surface (IRS) and derived an explicit and easy-to-implement solution for the IRS phase shifts. To make full use of the spatial DoFs and approach the upper bound of LoS capacity at any desired SNR, the authors of [8] proposed reconfigurable uniform linear arrays (ULAs) schemes to adapt spatial DoFs by means of rotating transceiver ULAs.

However, it can be observed that research on near-field LoS XL-MIMO channel modeling is still in its infancy. Most existing works, such as [7]–[9], utilize the geometry propagation model, which rely on accurate distance estimation between different transceiver antenna elements. However, acquiring this precise channel state information poses a significant challenge. Although [10] proposed a polar-domain representation for the near-field multiple-input-single-output (MISO) channel, it is invalid in LoS XL-MIMO scenarios since the receive cannot be viewed as a point from the transmit and vice versa. Recently, the authors of [11] proposed an EM-compliant representation for holographic MIMO scattering channels based on the plane wave decomposition. This approach effectively captures the essence of EM propagation and provides an efficient low-rank approximation for antenna-domain channel. Motivated by this, we endeavor to extend the plane wave decomposition method to near-field LoS MIMO channels.

Specifically, we first derive the angular-domain representation of the near-field LoS channel in the entire wavenumber space. Then, we analyze the structured sparsity exhibited by the resulting angular representation and unveil that a low-dimensional subspace is sufficient to effectively characterize the near-field LoS channel. To determine the effective subspace, we introduce the concept of effective spatial bandwidth, which quantifies the range of significant spatial frequencies between arrays, and propose an geometry-based identification method. Based on the effective spatial bandwidth, we derive a low-dimensional angular-domain representation for the near-field LoS channels, which characterizes the near-field LoS XL-MIMO channels as a superposition of multiple virtual far-field
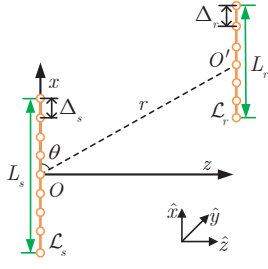
Fig. 1. XL-MIMO communication system with two parallel ULAs

LoS components, thereby capturing the spherical wavefront effect within a low-dimensional angular channel.

II. SYSTEM MODEL

Consider a point-to-point XL-MIMO communication system operating in the mmWave band as shown in Fig. 1. Two parallel and z-oriented linear arrays span the linear regions $\mathcal{L}_s$ and $\mathcal{L}_r$ of x-dimension L_s and L_r, respectively. The relative direction of the receive array placement is described by the angle $\theta \in (0, \pi)$ of the O-O' connecting line from the x-axis. Assume that N_t transmit antennas and N_r receive antennas are uniformly distributed in $\mathcal{L}_s$ and $\mathcal{L}_r$, respectively. Note that $\mathbf{s}_n = [s_{n,x}, s_{n,y}, s_{n,z}]^T \in \mathbb{R}^3$, $n = 1, \cdots, N_t$ and $\mathbf{r}_m = [r_{m,x}, r_{m,y}, r_{m,z}]^T \in \mathbb{R}^3$, $m = 1, \cdots, N_r$, are the coordinates of the n-th transmit antenna and the m-th receive antenna, respectively. The antenna spacing Δ_s and Δ_r in $\mathcal{L}_s$ and $\mathcal{L}_r$ are no greater than half of the wavelength. Due to the severe penetration loss incurred by the scatterers, we mainly consider the LoS channel between $\mathcal{L}_s$ and $\mathcal{L}_r$. Mathematically, the XL-MIMO system depicted in Fig. 1 can be expressed as

$$\mathbf{y} = \mathbf{H}\mathbf{x} + \mathbf{n}, \tag{1}$$

where $\mathbf{x} \in \mathbb{C}^{N_t}$ and $\mathbf{y} \in \mathbb{C}^{N_r}$ are the transmit and the receive signal vector, respectively; $\mathbf{H} \in \mathbb{C}^{N_r \times N_t}$ is the channel matrix; $\mathbf{n} \in \mathbb{C}^{N_r} \sim \mathcal{CN}(0, \sigma_N^2 \mathbf{I}_{N_r})$ denotes the additional white Gaussian noise with mean zero and variance σ_N^2.

Since the uniformly spaced antennas can be equivalently described as continuous apertures without losing accuracy [7], the analysis approach of EM theory can be incorporated. Assume that wave propagation takes place in the form of monochromatic scalar waves in free space and the reactive propagation mechanisms are excluded. The time-harmonic current density at the point $\mathbf{s} = [s_x, s_y, s_z]^T$ on $\mathcal{L}_s$ is $J(\mathbf{s})$, and the electric field at a generic position $\mathbf{r} = [r_x, r_y, r_z]^T$ on $\mathcal{L}_r$ is $E(\mathbf{r})$, which should satisfy the inhomogeneous Helmholtz equation, i.e.,

$$\nabla^2 E(\mathbf{r}) + k_0^2 E(\mathbf{r}) = -J(\mathbf{r}), \tag{2}$$

where $k_0 = 2\pi/\lambda$ is the wavenumber and $\nabla^2 = \frac{\partial^2}{\partial x^2} + \frac{\partial^2}{\partial y^2} + \frac{\partial^2}{\partial z^2}$ is the Laplacian operator.

The solutions of second-order partial differential equation (2) should satisfy [12]

$$E(\mathbf{r}) = \int_{\mathcal{L}_s} G(\mathbf{r} - \mathbf{s}) J(\mathbf{s}) d\mathbf{s}, \tag{3}$$

where $G(\mathbf{r} - \mathbf{s})$ denotes the scalar Green's function and is given by $G(\mathbf{r} - \mathbf{s}) = e^{jk_0 r}/4\pi r$ with $r = \|\mathbf{r} - \mathbf{s}\|$.

According to (3), we can see that the electric field at $\mathbf{r}$ is described as a superposition of wave components generated at point $\mathbf{s} \in \mathcal{L}_s$, which yields the spherical wavefront with a certain curvature. Intuitively, Green's function determines the LoS channel between $\mathcal{L}_s$ and $\mathcal{L}_r$ in free space [13]. Thus, the near-field LoS channel can be obtained by sampling $G(\mathbf{r}, \mathbf{s})$ at $\mathbf{s}_n$ and $\mathbf{r}_m$ for $n = 1, 2, \cdots, N_t$ and $m = 1, 2, \cdots, N_r$, i.e.,

$$[\mathbf{H}]_{mn} = \frac{\lambda}{4\pi r_{mn}} e^{jk_0 r_{mn}}, \tag{4}$$

with $r_{mn} = \|\mathbf{r}_m - \mathbf{s}_n\|$. According to the Friis's formula, the loss of free space depends on the communication distance and operating frequencies. Thus, we introduce the wavelength λ in (4), and $\lambda/4\pi r_{mn}$ determines the path gain between the m-th receive antenna and the n-th transmit antenna.

III. ANGULAR-DOMAIN REPRESENTATION OF NEAR-FIELD CHANNEL

A. Angular Representation for Near-Field Scattering Channels

According to Weyl's identity, a spherical wave can be decoupled into an infinite number of plane waves traveling to different directions [12]. The (m, n)-th entry of spatial channel $\mathbf{H}_c \in \mathbb{C}^{N_r \times N_t}$ in arbitrary scattering environments can be represented as [11]

$$[\mathbf{H}_c]_{mn} = \frac{1}{(2\pi)^2} \iiiint_{\mathcal{D}(k) \times \mathcal{D}(\kappa)} a_R(\kappa_x, \kappa_y, \mathbf{r}_m)$$
$$H_s(\kappa_x, \kappa_y, k_x, k_y) a_T^*(k_x, k_y, \mathbf{s}_n) dk_x dk_y d\kappa_x d\kappa_y, \tag{5}$$

where $a_T(k_x, k_y, \mathbf{s}_n)$ and $a_R(\kappa_x, \kappa_y, \mathbf{r}_n)$ are the source and receive response at $\mathbf{s}_n$ and $\mathbf{r}_m$, respectively, and are defined respectively as

$$a_T(k_x, k_y, \mathbf{s}_n) = e^{j\mathbf{k}^T \mathbf{s}_n} = e^{j(k_x s_{n,x} + k_y s_{n,y} + k_z s_{n,z})},$$
$$a_R(\kappa_x, \kappa_y, \mathbf{r}_m) = e^{j\boldsymbol{\kappa}^T \mathbf{r}_m} = e^{j(\kappa_x r_{m,x} + \kappa_y r_{m,y} + \kappa_z r_{m,z})}, \tag{6}$$

where $\mathbf{k} = [k_x, k_y, k_z]^T \in \mathbb{R}^3$ and $\boldsymbol{\kappa} = [\kappa_x, \kappa_y, \kappa_z]^T \in \mathbb{R}^3$ indicate the wave vectors of the transmit and receive plane-wave components with $k_z = (k_0^2 - k_x^2 - k_y^2)^{\frac{1}{2}}$ and $\kappa_z = (k_0^2 - \kappa_x^2 - \kappa_y^2)^{\frac{1}{2}}$. The parameter $H_s(\kappa_x, \kappa_y, k_x, k_y)$ is the coupling coefficient between the transmitted and received plane waves. Since we restrict the analysis to radiation near field and far field, the integration region is limited to $\mathcal{D}(k) = \{(k_x, k_y) : k_x^2 + k_y^2 \leq k_0^2\}$.

The formula (5) can be discretized to the superposition of finite sampling points, similar to the transition from the Fourier integral to the Fourier series. Assume the size of transmit (receive) array along x-axis and y-axis are denoted as $L_{T,x}$ and $L_{T,y}$ ($L_{R,x}$ and $L_{R,y}$). In this way, the wavenumber support $\mathcal{D}(k)$ ($\mathcal{D}(\kappa)$) can be partitioned with spacings $\Delta_{k_x} = 2\pi/L_{T,x}$ ($\Delta_{\kappa_x} = 2\pi/L_{R,x}$) and $\Delta_{k_y} = 2\pi/L_{T,y}$ ($\Delta_{\kappa_y} = 2\pi/L_{R,x}$) along k_x-axis (κ_x-axis) and k_y-axis (κ_y-axis) [11]. By rescaling the k_x (κ_x) and k_y (κ_y)-axis as

$k_x L_{T,x}/2\pi$ ($\kappa_x L_{R,x}/2\pi$) and $k_y L_{T,y}/2\pi$ ($\kappa_y L_{R,y}/2\pi$), these partitions of wavenumber space for transmit and receive array are indexed respectively by

$$\mathcal{S}_T = \left\{ (\xi_x, \xi_y) \in \mathbb{Z}^2 : \left(\frac{\lambda \xi_x}{L_{T,x}} \right)^2 + \left(\frac{\lambda \xi_y}{L_{T,y}} \right)^2 \leq 1 \right\},$$

$$\mathcal{S}_R = \left\{ (l_x, l_y) \in \mathbb{Z}^2 : \left(\frac{\lambda l_x}{L_{R,x}} \right)^2 + \left(\frac{\lambda l_y}{L_{R,y}} \right)^2 \leq 1 \right\}. \quad (7)$$

Denote $\varepsilon_{R,p} = (l_{x,p}, l_{y,p})$ and $\varepsilon_{T,q} = (\xi_{x,q}, \xi_{y,q})$ as the p-th and q-th entries of $\mathcal{S}_T$ and $\mathcal{S}_R$, (5) can be rewritten as

$$[\mathbf{H}_c]_{mn} \approx \sum_{p=1}^{S_R} \sum_{q=1}^{S_T} a_R(\varepsilon_{R,p}, \mathbf{r}_m) H_s(l_{x,p}, l_{y,p}, \xi_{x,q}, \xi_{y,q}) \quad (8)$$
$$\times a_T^*(\varepsilon_{T,q}, \mathbf{s}_n),$$

where $S_T = |\mathcal{S}_T|$ and $S_R = |\mathcal{S}_R|$ indicate the cardinalities of set $\mathcal{S}_T$ and $\mathcal{S}_R$; The parameter $H_s(l_{x,p}, l_{y,p}, \xi_{x,q}, \xi_{y,q})$ is the angular coupling coefficient and can be modeled as a random variable [12]; $a_R(\varepsilon_{R,p}, \mathbf{r}_m)$ and $a_T(\varepsilon_{T,q}, \mathbf{s}_n)$ are denoted respectively as

$$a_R(\varepsilon_{R,p}, \mathbf{s}_n) = \exp\left\{ j\left(\frac{2\pi}{L_{R,x}} l_{x,q} r_{m,x} + \frac{2\pi}{L_{R,y}} l_{y,q} r_{m,y} \right) \right\},$$
$$a_T(\varepsilon_{T,q}, \mathbf{r}_m) = \exp\left\{ j\left(\frac{2\pi}{L_{T,x}} \xi_{x,p} s_{n,x} + \frac{2\pi}{L_{T,y}} \xi_{y,p} s_{n,y} \right) \right\}. \quad (9)$$

For convenience, (8) can be rewritten in matrix form, i.e,

$$\mathbf{H}_c \approx \sqrt{N_t N_r} \sum_{p=1}^{S_R} \sum_{q=1}^{S_T} \mathbf{a}_R(\varepsilon_{R,p}) \mathbf{H}_s(p, q) \mathbf{a}_T(\varepsilon_{T,q})^H, \quad (10)$$

where $\mathbf{H}_s \in \mathbb{C}^{S_R \times S_T}$ denotes the angular channel matrix with $H_s(l_{x,p}, l_{y,p}, \xi_{x,q}, \xi_{y,q})$ as the (p, q)-th entry; $\mathbf{a}_R(\varepsilon_{R,p}) \in \mathbb{C}^{N_r}$ and $\mathbf{a}_T(\varepsilon_{T,q}) \in \mathbb{C}^{N_t}$ are the normalized response vectors corresponding to the p-th and q-th entries of $\mathcal{S}_R$ and $\mathcal{S}_T$, respectively, and they can be expressed respectively as

$$\mathbf{a}_R(\varepsilon_{R,p}) = \frac{1}{\sqrt{N_r}} [a_R(\varepsilon_{R,p}, \mathbf{r}_1), \cdots, a_R(\varepsilon_{R,p}, \mathbf{r}_{N_r})]^T,$$
$$\mathbf{a}_T(\varepsilon_{T,q}) = \frac{1}{\sqrt{N_t}} [a_T(\varepsilon_{T,q}, \mathbf{s}_1), \cdots, a_T(\varepsilon_{T,q}, \mathbf{s}_{N_t})]^T. \quad (11)$$

The formula (10) provides a low-rank approximation of the near-field scattering channels in the angular domain, which holds when $\min\{L_{R,x}, L_{R,y}\} \gg \lambda$ and $\min\{L_{T,x}, L_{T,y}\} \gg \lambda$. Inspired the low-rank approximation, we are also interested in angular-domain representation of near-field LoS channel.

B. Angular Representation for Near-Field LoS Channel

Compared to NLoS propagation, in the LoS scenario, the transmitted plane wave directly reaches the receive without alteration. Therefore, $\mathbf{k} = \boldsymbol{\kappa}$ can be obtained [12], which implies that there is a strong coupling between the transmitted and received plane waves with the same spatial frequency.

For the convenience of analysis, we utilize the same sampling spacing for $\mathcal{D}(k)$ and $\mathcal{D}(\kappa)$, i.e., $\Delta_{k_x} = \Delta_{\kappa_x} = 2\pi/L_{R,x}$

and $\Delta_{k_y} = \Delta_{\kappa_y} = 2\pi/L_{R,y}$ (assume $L_{R,x} \leq L_{T,x}$ and $L_{R,y} \leq L_{T,y}$), (7) can be rewritten as

$$\mathcal{S} = \left\{ (\xi_x, \xi_y) \in \mathbb{Z}^2 : \left(\frac{\lambda \xi_x}{L_{R,x}} \right)^2 + \left(\frac{\lambda \xi_y}{L_{R,y}} \right)^2 \leq 1 \right\}. \quad (12)$$

In the case of ULA, the component ξ_y can be further omitted. As a result, (12) reduces to $\mathcal{S} = \{\xi_x \in \mathbb{Z} : -1 \leq \frac{\lambda \xi_x}{L_{R,x}} \leq 1\}$ with $L_{R,x} = L_r$. Denote $\varepsilon_p = \xi_{x,p}$ and $\varepsilon_q = \xi_{x,q}$ the p-th and q-th entries of $\mathcal{S}$, the response vectors in (11) can be rewritten as

$$\mathbf{a}_R(\varepsilon_p) = \frac{1}{\sqrt{N_r}} [a_R(\varepsilon_p, \mathbf{r}_1), \cdots, a_R(\varepsilon_p, \mathbf{r}_{N_r})]^T,$$
$$\mathbf{a}_T(\varepsilon_q) = \frac{1}{\sqrt{N_t}} [a_T(\varepsilon_q, \mathbf{s}_1), \cdots, a_T(\varepsilon_q, \mathbf{s}_{N_t})]^T. \quad (13)$$

with

$$a_R(\varepsilon_p, \mathbf{r}_m) = \exp\left\{ j \frac{2\pi}{L_r} \xi_{x,p} r_{m,x} \right\},$$
$$a_T(\varepsilon_q, \mathbf{s}_n) = \exp\left\{ j \frac{2\pi}{L_r} \xi_{x,q} s_{n,x} \right\}. \quad (14)$$

Thus, the near-field LoS XL-MIMO channel can be decomposed as

$$\mathbf{H} \approx \sqrt{N_t N_r} \sum_{p=1}^{N_a} \sum_{q=1}^{N_a} \mathbf{a}_R(\varepsilon_p) \mathbf{H}_a(p, q) \mathbf{a}_T(\varepsilon_q)^H, \quad (15)$$

where $N_a = |\mathcal{S}|$ denote the cardinality of set $\mathcal{S}$; $\mathbf{H}_a(p, q)$ is the coupling coefficient between the p-th received plane wave and the q-th transmitted plane wave. Moreover, (15) can be rewritten more compactly as

$$\mathbf{H} \approx \sqrt{N_t N_r} \mathbf{A}_R \mathbf{H}_a \mathbf{A}_T^H, \quad (16)$$

with $\mathbf{A}_R = [\mathbf{a}_R(\varepsilon_1), \mathbf{a}_R(\varepsilon_2), \cdots, \mathbf{a}_R(\varepsilon_{N_a})]$ and $\mathbf{A}_T = [\mathbf{a}_T(\varepsilon_1), \mathbf{a}_T(\varepsilon_2), \cdots, \mathbf{a}_T(\varepsilon_{N_a})]$ indicating the stacked response matrices. Notably, $\mathbf{A}_T$ and $\mathbf{A}_R$ are semi-unitary matrices due to $N_a < \min\{N_t, N_r\}$.

Utilizing the semi-unitary property of transformation matrix $\mathbf{A}_T$ and $\mathbf{A}_R$, we have $\mathbf{H}_a \approx (1/\sqrt{N_t N_s}) \mathbf{A}_R^H \mathbf{H} \mathbf{A}_T$, which indicates that $\mathbf{H}_a$ and $\mathbf{H}$ are semi-unitarily equivalent. Thus, they should have identical significant singular values. To validate the observation, we provide some realizations of $\mathbf{H}_a$ for $N_t = N_r = 256$, $\Delta_s = \Delta_r = \lambda/2$, $\lambda = 0.01$m, and $r = 10$m, with the normalized eigenvalues shown in descending order in Fig. 2(a). As expected, it is observed that $\mathbf{H}$ and $\mathbf{H}_a$ have almost identical significant singular values for all the considered configurations. Furthermore, Fig. 2(b) illustrates that the significant entries of the angular-domain representation are confined to a specific subspace (within the red box). In other words, $\mathbf{H}_a$ offers a highly redundant description of the near-field LoS channel. To verify the idea, Fig. 2(c) quantifies the proportion of subspace power to the total angular channel power. It is evident that the majority of the channel power is concentrated in the subspace, with strong coupling occurring when the spatial frequency of the transmitted and received plane waves are the same. Notably, the coupling still exists between transmitted and received plane
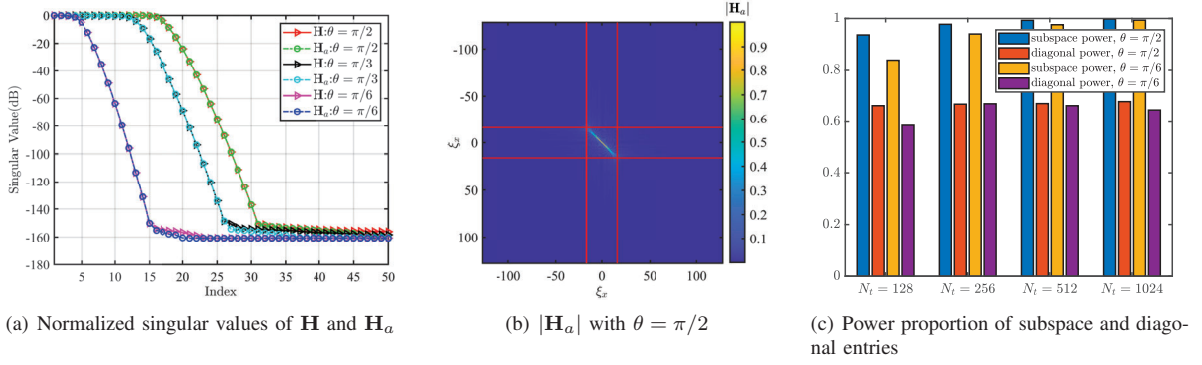
(a) Normalized singular values of $\mathbf{H}$ and $\mathbf{H}_a$

(b) $|\mathbf{H}_a|$ with $\theta = \pi/2$

(c) Power proportion of subspace and diagonal entries

Fig. 2. The characteristics of angular-domain channel with $\Delta_s = \Delta_r = \lambda/2$, $\lambda = 0.01$m, and $r = 10$m

waves with different spatial frequencies, which results in the diagonal entry power being less than the subspace power. In other words, the angular-domain channel $\mathbf{H}_a$ is not strictly diagonal, but diagonally dominant.

IV. PROPOSED LOW-DIMENSION REPRESENTATION FOR NEAR-FIELD LoS CHANNEL

Based on the previous analysis, it has been established that near-field LoS channel can be accurately represented using a subspace of $\mathcal{D}(k) \times \mathcal{D}(\kappa)$. To further investigate this subspace, we introduce the concept of effective spatial bandwidth between arrays in this section. Subsequently, we propose a low-dimension representation for near-field LoS channels.
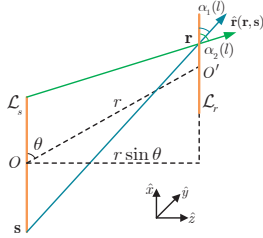

Fig. 3. Key parameters for clarifying spatial frequency and bandwidth

As shown in Fig. 3, any point $\mathbf{r}$ on $\mathcal{L}_r$ can be described as $l\hat{\mathbf{x}}$ with $l \in [-L_r/2, L_r/2]$. The spatial bandwidth of the perceived EM wave at point $\mathbf{r}$ is given by [6]

$$\omega(l, \mathcal{L}_s) = k_0 \left(\max_{\mathbf{s} \in \mathcal{L}_s} \hat{\mathbf{r}}^T(l, \mathbf{s})\hat{\mathbf{x}} - \min_{\mathbf{s} \in \mathcal{L}_s} \hat{\mathbf{r}}^T(l, \mathbf{s})\hat{\mathbf{x}} \right), \quad (17)$$

where $\hat{\mathbf{r}}^T(l, \mathbf{s})$ indicates the normalized direction vector from the source point $\mathbf{s} \in \mathcal{L}_s$ to the received point $\mathbf{r} = l\hat{\mathbf{x}}$. When $\mathcal{L}_s$ and $\mathcal{L}_r$ are parallel, the range of spatial frequencies at point $\mathbf{r}$ can be easily determined by the geometries of arrays. Obviously, $\max_{\mathbf{s} \in \mathcal{L}_s} \hat{\mathbf{r}}^T(l, \mathbf{s})\hat{\mathbf{x}}$ and $\min_{\mathbf{s} \in \mathcal{L}_s} \hat{\mathbf{r}}^T(l, \mathbf{s})\hat{\mathbf{x}}$ can be derived as $\cos\alpha_1(l)$ and $\cos\alpha_2(l)$, which are expressed respectively as

$$\begin{aligned} \cos\alpha_1(l) &= \frac{l+a}{\sqrt{(l+a)^2 + d^2}}, \\ \cos\alpha_2(l) &= \frac{l+b}{\sqrt{(l+b)^2 + d^2}}, \end{aligned} \quad (18)$$

with $d = r\sin\theta$, $a = r\cos\theta + L_s/2$, and $b = r\cos\theta - L_s/2$. As a result, (17) reduces to

$$\omega(l, r, \theta, L_s) = k_{\max}(l) - k_{\min}(l), \quad (19)$$

with $k_{\max}(l) = k_0 \cos\alpha_1(l)$ and $k_{\min}(l) = k_0 \cos\alpha_2(l)$. Consequently, the spatial bandwidth $\omega(m)$ for antenna m at $\mathbf{r}_m$ can be obtained by sampling $\omega(l, r, \theta, L_s)$ at $l = r_{x,m}$, $\forall m \in \{1, 2, \cdots, N_r\}$. Therefore, the *effective spatial bandwidth* between $\mathcal{L}_s$ and $\mathcal{L}_r$ in LoS scenarios is defined as

$$\omega_e = [\min_m k_{\min}(m), \max_m k_{\max}(m)], \forall m. \quad (20)$$

Once the range of effective spatial bandwidth is determined, it can be discretized to finite sampling points through partitioning ω_e with spacing $2\pi/L_r$, i.e.,

$$\mathcal{S}_e = \{\xi_x : k_{\min}^e \le \frac{2\pi\xi_x}{L_r} \le k_{\max}^e\}. \quad (21)$$

Let $\sin\vartheta_p = 2\pi\xi_{x,p}/L_r k_0$, $\forall \xi_{x,p} \in \mathcal{S}_e, p = 1, 2, \cdots, N_e$, where $N_e = |\mathcal{S}_e|$ indicates the cardinality of set $\mathcal{S}_e$. As a result, the source and receive response corresponding to spatial frequency $2\pi\xi_{x,p}/L_r$ can be written respectively as

$$\begin{aligned} [\mathbf{a}_T(\vartheta_p)]_n &= \frac{1}{\sqrt{N_t}} e^{j\frac{2\pi}{\lambda}n\Delta_s \sin\vartheta_p}, \\ [\mathbf{a}_R(\vartheta_p)]_m &= \frac{1}{\sqrt{N_r}} e^{j\frac{2\pi}{\lambda}m\Delta_r \sin\vartheta_p}. \end{aligned} \quad (22)$$

Consequently, the near-field LoS channel for XL-MIMO can be expressed as

$$\mathbf{H} \approx \sqrt{N_t N_r} \sum_{p=1}^{N_e} \sum_{q=1}^{N_e} \mathbf{a}_R(\vartheta_p) \mathbf{H}_a^e(p, q) \mathbf{a}_T^H(\vartheta_q), \quad (23)$$

where $\mathbf{H}_a^e(p, q)$ is the angular channel coefficient between the p-th received plane wave with spatial frequency $2\pi\xi_{x,p}/L_r$ and the q-th transmitted plane wave with spatial frequency $2\pi\xi_{x,q}/L_r$. It is interesting to see that (23) have similar structure as the conventional far-field SV channel model, where the angle of departure (AOD) and angle of arrival (AOA) of each path are ϑ_q and ϑ_p, respectively. Moreover, the channel model in (23) can be rewritten more compactly as

$$\mathbf{H} \approx \sqrt{N_t N_r} \mathbf{A}_R^e \mathbf{H}_a^e (\mathbf{A}_T^e)^H, \quad (24)$$

(a) Normalized $|\mathbf{H}_a|$ and $|\mathbf{H}_a^e|$

(b) Normalized singular values of $\mathbf{H}$, $\mathbf{H}_a$, and $\mathbf{H}_a^e$
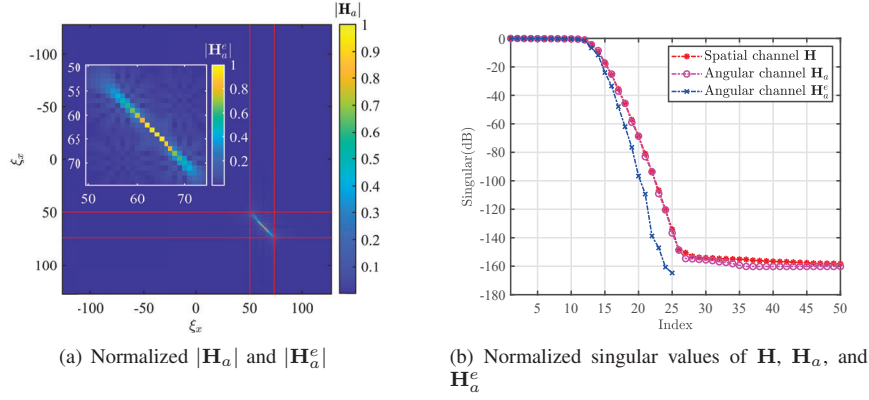
Fig. 4. Normalized $|\mathbf{H}_a|$, $|\mathbf{H}_a^e|$ and singular values with $N_t = N_r = 256$, $\Delta_s = \Delta_r = \lambda/2$, $\lambda = 0.01$m, $r = 10$m, and $\theta = \pi/3$

with $\mathbf{A}_T^e = [\mathbf{a}_T(\vartheta_1), \cdots, \mathbf{a}_T(\vartheta_{N_e})]$ and $\mathbf{A}_R^e = [\mathbf{a}_R(\vartheta_1), \cdots, \mathbf{a}_R(\vartheta_{N_e})]$.

Furthermore, when we only consider the strong coupling between transmitted plane wave and received plane wave with the same spatial frequency, (23) can is reduced to

$$\mathbf{H} \approx \sqrt{N_t N_r} \sum_{p=1}^{N_e} g_p \mathbf{a}_R(\vartheta_p) \mathbf{a}_T^H(\vartheta_p), \qquad (25)$$

where g_p denotes the coupling between transmitted plane wave and received plane wave with the spatial frequency $2\pi\xi_{x,p}/L_r$.

The formulation presented in (23) or (25) reveals that the near-field LoS channel can be effectively modeled as a superposition of multiple virtual far-field LoS components using the plane wave decomposition technique within the effective spatial bandwidth. The representation captures the spherical wavefront effect in a low-dimension angular channel without loss of spatial DoFs, which significantly deviates from the rank-1 LoS channel representation with plane wavefront assumption.

V. SIMULATION RESULTS

A. The Equivalence of Different Channel Representations

Fig. 4(a) shows the normalized angular matrices $|\mathbf{H}_a|$ and $|\mathbf{H}_a^e|$ with parameters $N_t = N_r = 256$, $\Delta_s = \Delta_r = \lambda/2$, $\lambda = 0.01$m, $r = 10$m, and $\theta = \pi/3$. According to (20), $\mathcal{S} = \{50, 51, \cdots, 74, 75\}$ at this time, which is consistent with the range of the red box. This verifies the effectiveness of the identification method of effective spatial bandwidth. In addition, it can be observed that the entries of $|\mathbf{H}_a|$ and $|\mathbf{H}_a^e|$ in the red box are nearly identical, which confirms the equivalence between $\mathbf{H}_a$ and $\mathbf{H}_a^e$. Furthermore, Fig. 4(b) presents that the normalized singular values of $\mathbf{H}$, $\mathbf{H}_a$, and $\mathbf{H}_a^e$ are nearly identical, indicating that $\mathbf{H}_a^e$ is equivalent to $\mathbf{H}$ and the spherical wavefront effect is well embedded in the angular channel. Thus, we can utilize $\mathbf{H}_a^e$ to characterize the near-field LoS without losing any essential information.

Consequently, compared with $\mathbf{H}_a$ and $\mathbf{H}$, the dimensions of $\mathbf{H}_a^e$ can be significantly reduced. TABLE. I compares the dimensions of antenna-domain channel and angular channel

with $\Delta_s = \Delta_r = \Delta$, $\theta = \pi/2$ and $r = 10$m. For example, when $\Delta = \lambda/2$, $\lambda = 0.01$m, $N_t = N_r = 256$, $\theta = \pi/2$, and $r = 10$m, the dimensions of the angular channel matrix $\mathbf{H}_a$ are almost equal to the number of antennas, whereas the dimensions of $\mathbf{H}_a^e$ are reduced to 33×33. The low-dimension representation will significantly facilitate the acquisition of channel state information and reduce the complexity of signal processing in XL-MIMO systems.

B. The Effects of Array Geometries on Effective Spatial Bandwidth

We first investigate the effective spatial bandwidth under different antenna spacings with fixed array sizes, assuming $\Delta_s = \Delta_r = \Delta$ for simplicity. Other parameters are as follows: $L_s = L_r = 100\lambda$, $\lambda = 0.01$m, $r = 10$m, and $\theta = \pi/3$. Fig. 5 shows that the significant entries of $\mathbf{H}_a$ and $\mathbf{H}_a^e$ are nearly identical for different antenna spacings, which indicates that the effective spatial bandwidth and spatial DoFs between $\mathcal{L}_s$ and $\mathcal{L}_r$ do not increase beyond a certain threshold as the number of antennas increases.

We further investigate the effects of array size on the effective spatial bandwidth with $N_t = N_r = 512$, $\lambda = 0.01$m, $r = 10$m, and $\theta = \pi/3$. Fig. 6 shows that the effective spatial bandwidth increases with the array size. This can be attributed to the fact that increasing the source array size tends to increase the local spatial bandwidth, while increasing the receiving array size tends to increase the observation interval. Thus, increasing the size of the source and/or receiving array tends to increase the effective spatial bandwidth and the available spatial DoFs.

VI. CONCLUSION

In this paper, the low-dimension angular-domain representation of near-field LoS channel has been investigated. Due to the LoS propagation and finite array size, the power of the angular channel is only concentrated on an effective subspace of the entire wavenumber space, where strong coupling occurs when the spatial frequency of the transmitted and received plane waves are the same. Based on the structured sparsity, we proposed a geometry-based method to identify the effective

TABLE I: The dimension comparison of space-domain channel and angular channel

Channel Matrix	Sampling Dimension	Antenna Spacing			
		$\lambda/2$		$\lambda/4$	
$\mathbf{H}$	$N_r \times N_t$	128×128	256×256	128×128	256×256
$\mathbf{H}_a$	$N_a \times N_a$	127×127	255×255	64×64	128×128
$\mathbf{H}_a^e$	$N_e \times N_e$	9×9	33×33	3×3	9×9

(a) $\Delta = \lambda/8$ (b) $\Delta = \lambda/4$ (c) $\Delta = \lambda/2$
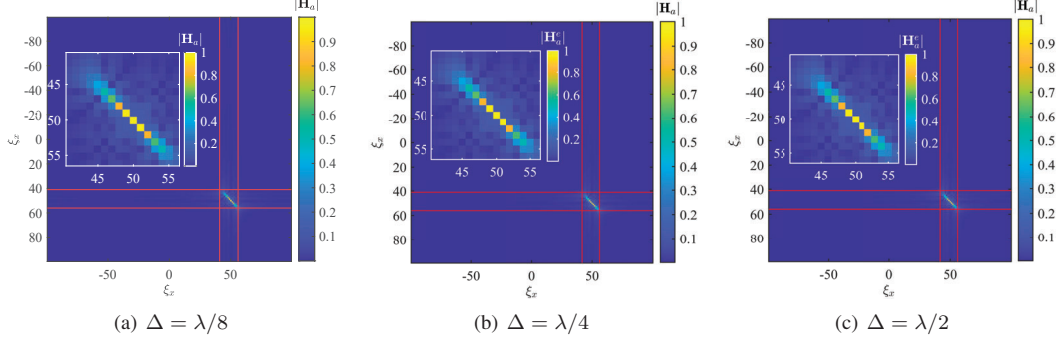
Fig. 5. Effective spatial bandwidth versus Δ with $L_s = L_r = 100\lambda$, $\lambda = 0.01$m, $r = 10$, and $\theta = \pi/3$

(a) $\Delta = \lambda/8$ (b) $\Delta = \lambda/4$ (c) $\Delta = \lambda/2$
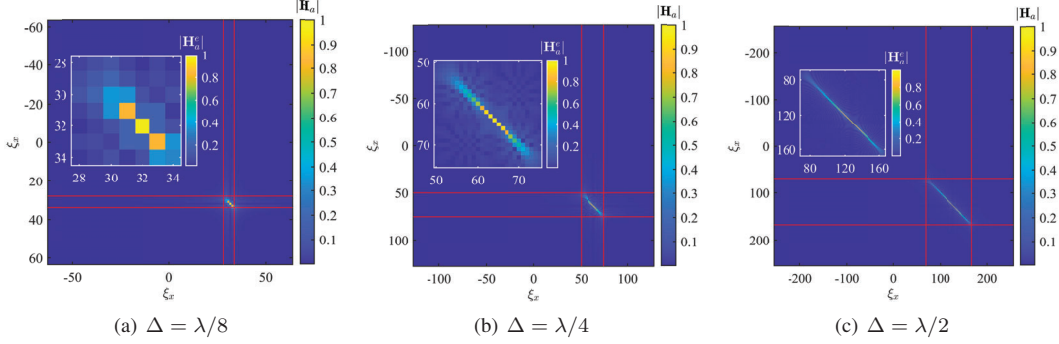
Fig. 6. Effective spatial bandwidth versus Δ with $N_t = N_r = 512$, $\lambda = 0.01$m, $r = 10$, and $\theta = \pi/3$

subspace and derived a low-dimension angular-domain representation which characterizes the near-field LoS channel as a superposition of multiple virtual far-field LoS components. In addition, through simulations, we have verified the equivalence of different channel representations and evaluated the effects of array geometries on the effective spatial bandwidth.

REFERENCES

[1] H. Tataria, M. Shafi, A. F. Molisch, M. Dohler, H. Sjöland, and F. Tufvesson, "6G wireless systems: Vision, requirements, challenges, insights, and opportunities," *Proceedings of the IEEE*, vol. 109, no. 7, pp. 1166–1199, 2021.

[2] Y. F. L. M. TANG Junwen, XU Shenheng, "Recent developments of transmissive reconfigurable intelligent surfaces: A review," *ZTE Communications*, vol. 20, no. 1, p. 21, 2022. [Online]. Available: http://zte.magtechjournal.com/EN/abstract/article_718.shtml

[3] H. Zhang, N. Shlezinger, F. Guidi, D. Dardari, M. F. Imani, and Y. C. Eldar, "Beam focusing for near-field multiuser MIMO communications," *IEEE Transactions on Wireless Communications*, vol. 21, no. 9, pp. 7476–7490, 2022.

[4] Y. Pan, K. Wang, C. Pan, H. Zhu, and J. Wang, "Sum-rate maximization for intelligent reflecting surface assisted terahertz communications," *IEEE Transactions on Vehicular Technology*, vol. 71, no. 3, pp. 3320–3325, 2022.

[5] D. Dardari, "Communicating with large intelligent surfaces: Fundamental limits and models," *IEEE Journal on Selected Areas in Communications*, vol. 38, no. 11, pp. 2526–2537, 2020.

[6] L. Ding, E. G. Ström, and J. Zhang, "Degrees of freedom in 3D linear large-scale antenna array communications—a spatial bandwidth approach," *IEEE Journal on Selected Areas in Communications*, vol. 40, no. 10, pp. 2805–2822, 2022.

[7] H. Do, N. Lee, and A. Lozano, "Line-of-sight mimo via intelligent reflecting surface," *IEEE Transactions on Wireless Communications*, pp. 1–1, 2022.

[8] Do, Heedong and Lee, Namyoon and Lozano, Angel, "Reconfigurable ulas for line-of-sight mimo transmission," *IEEE Transactions on Wireless Communications*, vol. 20, no. 5, pp. 2933–2947, 2021.

[9] E. Torkildson, U. Madhow, and M. Rodwell, "Indoor millimeter wave mimo: Feasibility and performance," *IEEE Transactions on Wireless Communications*, vol. 10, no. 12, pp. 4150–4160, 2011.

[10] M. Cui and L. Dai, "Channel estimation for extremely large-scale MIMO: Far-field or near-field?" *IEEE Transactions on Communications*, vol. 70, no. 4, pp. 2663–2677, 2022.

[11] A. Pizzo, L. Sanguinetti, and T. L. Marzetta, "Fourier plane-wave series expansion for holographic MIMO communications," *IEEE Transactions on Wireless Communications*, vol. 21, no. 9, pp. 6890–6905, 2022.

[12] A. Pizzo, L. Sanguinetti, and T. L. Marzetta, "Spatial characterization of electromagnetic random channels," *IEEE Open Journal of the Communications Society*, vol. 3, pp. 847–866, 2022.

[13] A. Pizzo and A. Lozano, "On landau's eigenvalue theorem for line-of-sight MIMO channels," *IEEE Wireless Communications Letters*, vol. 11, no. 12, pp. 2565–2569, 2022.